Ecological Archives E091-104-A1

Leo Polansky, George Wittemyer, Paul C. Cross, Craig J. Tambling, and Wayne M. Getz. 2010. From moonlight to movement and synchronized randomness: Fourier and wavelet analyses of animal location time series data. Ecology 91:1506-1518.

Appendix A. The Appendix contains: 1) details on the Fourier and wavelet methods; 2) additional details on the method of simulation; 3) more extensive simulation studies to evaluate issues of sampling interval size and to show that the results presented in Fig. 4 of the main text are not an artifact of the particular movement trajectory used; 4) additional analyses and results of the lion and buffalo data; 5) a table summarizing the parameters used in the implementation of the frequency and time-frequency methods for each data set.

A1. Fourier and wavelet methods

Fourier analysis is a ubiquitous tool throughout science, *inter alia* allowing estimation of the strength of frequencies ω making up the spectral density $f(\omega)$ of a stationary stochastic process. Computational strategy takes $\omega_k = k/N$, for $k = 0,\ldots,N\text{-}1$ as a set of suitable frequencies from which to estimate $f(\omega)$. The discrete Fourier transform of the time series $\mathbf{X}^N$ at frequency ω_k is defined as

$$\hat{I}(\omega_k) = \frac{1}{N}\sum_{j=0}^{N-1} X_j e^{-2i\pi kj/N}, \quad \text{(Eq. A1)}$$

and provides a means to estimate the spectral density with the raw periodogram, or sample power spectral density, defined as $\hat{f}(\omega) = \left|\hat{I}(\omega)\right|^2$. The periodogram $\hat{f}(\omega)$ will show peaks in its power at frequencies most correlated with the data.

There are many widely recognized theoretical advantages of Fourier analysis (see e.g. Brillinger 1981 or Shumway and Stoffer 2000), two of which in particular provide convenient approaches for testing empirical movement data against null random walk models. First, an exact analytic relationship exists between both independent identically distributed (i.i.d.) normal distributions (white noise) and AR(1) (red noise) models and their spectral densities (Gilman et al. 1963, Shumway and Stoffer 2000). Second, the knowledge that $2\hat{f}(\omega_k)/f(\omega)$, where ω is close to ω_k, is asymptotically chi-squared distributed with two degrees of freedom (Shumway and Stoffer 2000) guides significance testing by providing asymptotic test statistics from which to estimate a confidence envelope around the estimated spectrum. Note that the dependence of the periodogram values on ω_k alone (but not on t_j) and integration over time in Eq. A1 reflects the stationarity assumption, inhibiting it from detecting changes in the frequency content of $\mathbf{X}^N$ as a function of time t_j. For this, task, we can employ wavelet analysis. Finally, software (e.g. the R environment) and strategies (Press et al. 2007) for estimating the spectral density from the periodogram are highly developed .

Wavelet analysis allows temporally local estimation of dominant frequencies correlated with $\mathbf{X}^N$ by employing functions (wavelets) that are dilated or contracted versions of an analyzing wavelet (function) ψ, translated across the time series. Wavelet analysis has an interesting literature and theory that we do not review here, discussing only the necessary motivating material and referring readers to Blatter (1998), Torrence and Compo (1998) or Carmona et al. (1998) for introductions to this topic, or any of Cazelles et al. (2007), Cazelles et al. (2008), or

Dong et al. (2008) for recent reviews oriented towards the biological sciences. The continuous wavelet transform with L^2-normalization of the discrete time series $\mathbf{X}^N$ at scale a and time t_i is defined by

$$W\left[a, t_j\right] = \frac{1}{\sqrt{a}} \sum_{l=1}^{N} X_j \psi^* \left[\frac{(l-j)\Delta t}{a}\right] \quad \text{(Eq. A2)}$$

where ψ^* denotes the complex conjugate of the analyzing wavelet function ψ. We use the Morlet wavelet function $\psi(\eta) = \pi^{-1/4}\exp(-i\omega_0\eta)\exp(-\eta^2/2)$, where ω_0 controls the oscillation frequency. Choosing ω_0 to be 2π, as is done in our analyses, preserves an approximate inverse relationship between the frequency of the power spectrum of a Fourier analysis and scale of wavelet transform (Maraun and Kurths 2004). As with all applications of these methods in practice, the choice of scales (frequencies) is a set of discrete values, typically defined by $a_k = s_0 2^{k\Delta k}$, $k = 0,1,\ldots,K$, where $s_0 = 2\Delta t$, and Δk and K depend on the analyzing wavelet, length and resolution of the data (Torrence and Compo 1998). The estimated wavelet power spectrum of $\mathbf{X}^N$ (also called the scalogram) is defined as the data array of squared modulus values $\hat{\mathbf{W}} = \left|W[a_k, t_j]\right|^2, j = 0,1,\ldots,N\text{-}1$, $k = 0,1,\ldots,K$, and provides an estimate of the true wavelet spectrum. Averaging the scalogram in both the time and scale directions will reduce the variance of the estimate but increases its bias (Torrence and Compo 1998, Maraun et al. 2007).

Two features of the scalogram are necessary to consider when evaluating significance of scalogram values. First, in contrast with significance testing of periodogram values, estimating significance of scalogram values relies exclusively on bootstrapping (Torrence and Compo 1998). For example, to test if a velocity time series is different from white or red noise, one would estimate the white and red noise parameters from $\mathbf{X}^N$ to generate a large number of replicate velocity time series and estimate quantiles for each modulus value $\left|W[a_k, t_j]\right|^2$. Second,

the cone-of-influence that demarcates the region of the scalogram in which edge effects on the scalogram are present (due to zero padding the original data for computational efficiency) is dependent on the choice of analyzing wavelet ψ and the scale a_k (Torrence and Compo 1998). Since modulus values outside this cone-of-influence have been influenced by these edge effects, these values should be disregarded for purpose of statistical inference and cautiously interpreted biologically.

There are at least two potentially useful pieces of information that can be extracted from wavelet transforms. Both use a wavelet Parseval formula (Blatter 1998) which relates the total variance σ^2 of $\mathbf{X}^N$ to its scalogram through the double integral $\sigma^2 = \frac{1}{C_\psi N} \iint_{RxR^*} \frac{\left|W\left[a,t\right]\right|^2}{a^2} dtda$, where C_ψ is the wavelet specific constant $C_\psi = \int \frac{|\hat{\psi}(\omega)|^2}{\omega} d\omega$ (Blatter 1998, Torrence and Compo 1998), where $\hat{\psi}(\omega)$ denotes the Fourier transform of ψ. The first is a time series of percent variance explained by a band of frequencies from a_{j_1} to a_{j_2}, at time t_j, which is calculated as $\sigma^2_{\text{per}}(t_j) = \frac{1}{A} \sum_{k=j_1}^{k=j_2} \frac{|W[a_k,t_j]|^2}{a_k}$, where $A = \sum_{j=0}^{N} \sum_{k=0}^{k=K} \frac{|W[a_k,t_j]|^2}{a_k}$ is a normalizing constant. Peaks from the periodogram would be a natural first choice in selecting frequencies to investigate the σ^2_{per} function. Second, the time series of percent variance explained in autocorrelative patches at each time t_j, $\sigma^2_{sig}(t_j) = \frac{1}{A} \sum_{k=0}^{k=K} \frac{\delta(a_k)\,|W[a_k,t_j]|^2}{a_k}$, where $\delta(a_k)$ is a Dirac measure taking on the value of 1 when a_k is inside a significant patch (warm colored areas in the scalogram), may be useful for detecting qualitative trends in the proportion of frequencies with significant complex autocorrelation compared to those of red or white noise (Wittemyer et al. 2008). For any investigations of velocity data, however, it is important to acknowledge that both of these

statistics are somewhat compromised by the finite nature of the data and correlations of the modulus values in the time and scale directions (Maraun et al. 2007).

With two contiguous time series, cross wavelet analysis can aid in comparing the time-specific movements of two individuals. Let $\hat{\mathbf{W}}_1$ and $\hat{\mathbf{W}}_2$ denote the scalograms for the time series $\mathbf{X}_1^N$ and $\mathbf{X}_2^N$ of two separate individuals with the same sampling parameters, respectively. The wavelet cross spectrum is estimated as $WCS_{1,2}[a_k, t_j] = \left\langle \hat{\mathbf{W}}_1[a_k, t_j], \hat{\mathbf{W}}_2^*[a_k, t_j] \right\rangle$, where * denotes the complex conjugate, and the wavelet coherency is estimated as

$$WCO_{1,2} = \frac{\left\| S(WCS_{1,2}) \right\|}{\left\| S(\hat{\mathbf{W}}_1) \right\|^{1/2} \left\| S(\hat{\mathbf{W}}_2) \right\|^{1/2}}, \quad \text{(Eq. A3)}$$

where S denotes a smoothing operator. Using the Morlet wavelet $WCS_{1,2}$ is complex. Thus, we can obtain both the strength of correlation between the two individuals from the modulus squared values $\left|WCO_{1,2}\right|^2$, ranging from 0 to 1, with 1 denoting a linear relationship, and 0 denoting no relationship, and the phase lag between them (measured in radians from $-\pi$ to π). Smoothing in the time and scale dimensions is essential when computing Eq. A3 (see Maraun and Kurths 2004 for details).

A2. Stochastic Simulation

For ease of notation, we will assume there is only one type of behavior in the time interval [t_i, t_{i+1}], allowing us to ignore τ_k and drop the subscripts on $\mathbf{m}$, $\boldsymbol{\mu}$, $\boldsymbol{\sigma}$. The starting point is the general stochastic differential equation

$$\mathbf{r}(t) = \mathbf{r}(0) + \int_0^t \boldsymbol{\mu}\big(\mathbf{r}(s), s\big)\mathrm{d}s + \int_0^t \boldsymbol{\sigma}\big(\mathbf{r}(s), s\big)\mathrm{d}\mathbf{B}\big(s\big) \quad \text{(Eq. A4)}$$

in time s and space $\mathbf{r}(s)$. Different methods for simulating solutions from Eq. A4 exist, depending on the functional forms for the drift $\boldsymbol{\mu}$ and diffusion $\boldsymbol{\sigma}$ functions (Iacus 2008). Under the assumptions of constant drift $\boldsymbol{\mu} = (\mu, \mu)$ and diffusion $\boldsymbol{\sigma} = (\sigma, \sigma)$, for scalar values μ and σ, Eq. A4 reduces to

$$\mathbf{r}(t) = \mathbf{r}(0) + \int_0^t \boldsymbol{\mu} ds + \int_0^t \boldsymbol{\sigma} d\mathbf{B}(s) \quad \text{(Eq. A5)}$$

the Euler method is suitable for the goal of obtaining a stochastic movement trajectory from Eq. A5. Other methods (e.g. the various Milstein schemes) discussed in Iacus (2008) that increase approximation accuracy with the inclusion of second-order terms in the approximation of the drift and diffusion are equivalent to the Euler method in this case because of the assumed constancy of the drift and diffusion.

To simulate trajectories from Eq. A5, we obtained a random time t_{i+1} in minutes uniformly distributed on the interval [30 minutes, 90 minutes]. We then divided the interval $[t_i, t_{i+1}]$ into half minute increments during which the Weiner process $\mathbf{B}(s)$ was assumed constant with mean 0 and standard deviation $\sqrt{0.5}$ from which to obtain displacement in $\mathbf{r}(s)$. By repeating this process an appropriate number of times, and changing the values of μ and σ when necessary, we obtained movement trajectories from which to obtain sampled data from. Figure A1 shows the simulated and sampled paths and associated velocity of the movement trajectory used for producing Fig. 4 of the main text.

A3. Additional simulation studies

There are several main objectives of the objectives of additional simulation study: i) include some simulations and discussion on the role of sampling interval Δt; and ii) simulate multiple movement trajectories for all synthetic scenarios to illustrate that the results are not an artifact of

the particular time series used to illustrate sample periodograms and scalograms. The results are shown in Figs. A2-A5, which confirm the utility of the methods discussed in the main text even at coarser sampling intervals, although the ability to detect locations of changes in the daily behavioral sequence does erode considerably, and demonstrate that the results are not an artifact of the particular time series shown in Fig. A1 used in the analysis summarized in Fig. 4 of the main text.

A4. Additional lion and buffalo analyses

This section presents a summary (Table A1) and additional analyses and figures of the empirical data.

For the lion dataset, the additional analyses are the correlation of movement with moonlight intensity and the scalogram value at the frequency $\omega = 1$ cycle/day. The results are shown in figure A6.

The African buffalo data set consists in total of six individuals (Table A1). Each individual showed irregular crepuscular activity (Figs. A7-A12) and an associated peak at $\omega = 2$ cycles/day in their periodogram, with individuals T12, T13, T16 and T17 also showing some additional activity around midnight, resulting in $\omega = 3$ cycles/day dominating the periodogram (Figs. A8, A9, A11, A12). Two groups of three (T12, T13, T16 and T7, T15, T17, see table A1) overlapped in time sufficiently to conduct wavelet coherency analyses (Fig. 6 in the main text and Figs. A13-A17 of the appendix). Of the 6 pairs, two pairs (those formed by combining T17 with either T7 or T15) did not come close enough to compare movement statistics associated with within and between herds. The significant patches emerging in the wavelet coherence analyses for these pair (Figs. A16-A17) are likely spurious based on both consideration of biological dynamics, the

other four data sets for which fission-fusion dynamics are recorded, a examination of wavelet coherency patterns for simulated data sets in which there are no random walks across days (Fig. A18), a considerably more overall cyclical movement pattern than shown in the buffalo (Table 1 of the main text). Of the four pair that involved fission-fusion herding events, all pairs clearly showed synchrony at distances of approximately less than 1 km (Figs. A19-A22).

Table A1- Summaries of empirical data. All individuals were sampled with an interval of 1 hour.

Data set	Start date and time	End date and time	velocity data sample size	percent velocity data missing
Lion	5/19/05 22:12	11/17/05 1:38	4347	25
Buffalo data sets				
T7	9/15/05 9:41	1/11/06 7:47	2830	6
T12 (individual 1 presented in main text)	7/14/05 14:35	12/8/05 0:16	3514	<1
T13 (individual 2 presented in main text)	7/15/05 9:02	10/29/05 20:49	2555	<1
T15	9/15/05 16:06	12/27/05 4:23	2460	7
T16	7/27/05 9:06	10/8/05 5:57	1748	6
T17	8/23/05 7:34	4/20/06 18:09	5770	<1

A5. Table of parameters used in the implementation of frequency and time-frequency analyses

For smoothing the Fourier periodograms, we used a modified Danielle smoother (Shumway and Stoffer 2000) as implement in R 2.6.2. Table A1 lists the number of adjacent data points

included in this smoother in both the positive and negative directions. Wavelet based analyses require additional choices about the range of scales, determined by the octave and voice parameters, and smoothing in both the time and frequency directions (Torrence and Compo 1998, Maraun and Kurths 2004).

Table 2- Summary of parameters used in implementing frequency and time-frequency methods.

Data set	Fourier method	Wavelet method			
	Frequency smoothing	Number of octaves	Number of voices	Smoothing in scale	Smoothing in time
Simulated data	Adjacent 3 points	8	24	0	0
Lion data	Adjacent 3 points	8	24	0	0
Buffalo data sets					
T7	Adjacent 3 points	8	24	0	0
T12	Adjacent 3 points	8	24	0	0
T13	Adjacent 3 points	8	24	0	0
T15	Adjacent 3 points	8	24	0	0
T16	Adjacent 3 points	8	24	0	0
T17	Adjacent 3 points	9	24	0	0
T12 cross T13	-	8	24	0.5	2
T12 cross T16	-	8	24	0.5	2
T13 cross T16	-	8	24	0.5	2
T7 cross T15	-	8	24	0.5	2
T7 cross T17	-	8	24	0.5	2
T15 cross T17	-	8	24	0.5	2

Appendix literature cited

Blatter, C. 1998. Wavelets A Primer. A K Peters, Ltd., Natick, MA.

Brillinger, D. R. 1981. Time series: data analysis and theory. Expanded edition. Holden-Day, San Francisco.

Carmona, R., H. Wen-Liang, and B. Torresani. 1998. Practical time-frequency analysis: Garbor and wavelet transforms with an implementation in S. Academic Pres, San Diego, Ca.

Cazelles, B., M. Chavez, D. Berteaux, F. Menard, J. O. Vik, S. Jenouvrier, and N. C. Stenseth. 2008. Wavelet analysis of ecological time series. Oecologia **156**:287-304.

Cazelles, B., M. Chavez, G. C. de Magny, J. F. Guegan, and S. Hales. 2007. Time-dependent spectral analysis of epidemiological time-series with wavelets. Journal of the Royal Society Interface **4**:625-636.

Dong, X. J., P. Nyren, B. Patton, A. Nyren, J. Richardson, and T. Maresca. 2008. Wavelets for agriculture and biology: A tutorial with applications and outlook. Bioscience **58**:445-453.

Gilman, D. L., F. J. Fuglister, and J. M. Mitchell. 1963. On the power spectrum of red noise. Journal of the Atmospheric Sciences **20**:182-184.

Iacus, S. M. 2008. Simulation and inference for stochastic differential equations with R examples. Springer, New York, NY.

Maraun, D., and J. Kurths. 2004. Cross wavelet analysis: significance testing and pitfalls. Nonlinear Processes in Geophysics **11**:505-514.

Maraun, D., J. Kurths, and M. Holschneider. 2007. Nonstationary Gaussian processes in wavelet domain: Synthesis, estimation, and significance testing. Physical Review E **75**.

Press, W. H., Saul A. Teukolsky, William T. Vetterling, Brian P. Flannery. 2007. Numerical Recipes: The Art of Scientific Computing. Third edition. Cambridge Univesity Press, New

York, NY.

R Devlopment Core Team. 2008. R: A language and environment for statistical computing. R Foundation for Statistical Computing, Vienna, Austria. http://R-project.org.

Shumway, R. H., and D. S. Stoffer. 2000. Time Series Analysis and Its Applications. 1st edition. Springer-Verlag, Harrisonburg, VA.

Torrence, C., and G. P. Compo. 1998. A practical guide to wavelet analysis. Bulletin of the American Meteorological Society **79**:61-78.

Wittemyer, G., L. Polansky, I. Douglas-Hamilton, and W. M. Getz. 2008. Disentangling the effects of forage, social rank, and risk on movement autocorrelation of elephants using Fourier and wavelet analyses. Proceedings of the National Academy of Sciences **105**:19108-19113.

Figure A1

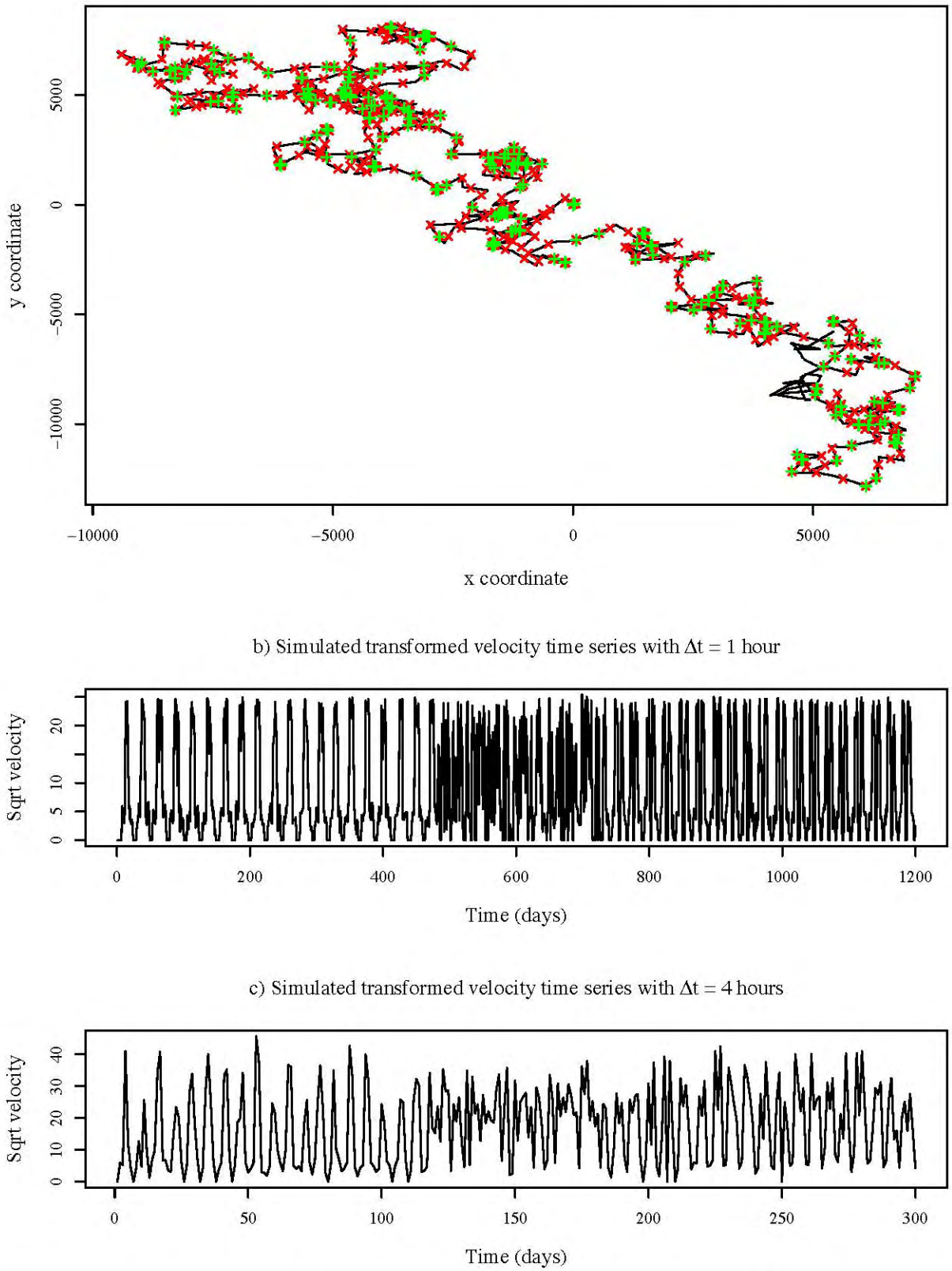

Figure A1. (a) Spatial plot and velocity time series for the data analyzed in Fig. 4 of the main text. The black line is the continuous path, red crosses show locations as recorded every 1 hour and green pluses show 4-hour sampled locations. The square root transformed velocity time series for the 1-hour sampled data is shown in panel (b) and the square root transformed velocity time series for the 4-hour sampled data is shown in panel (c).

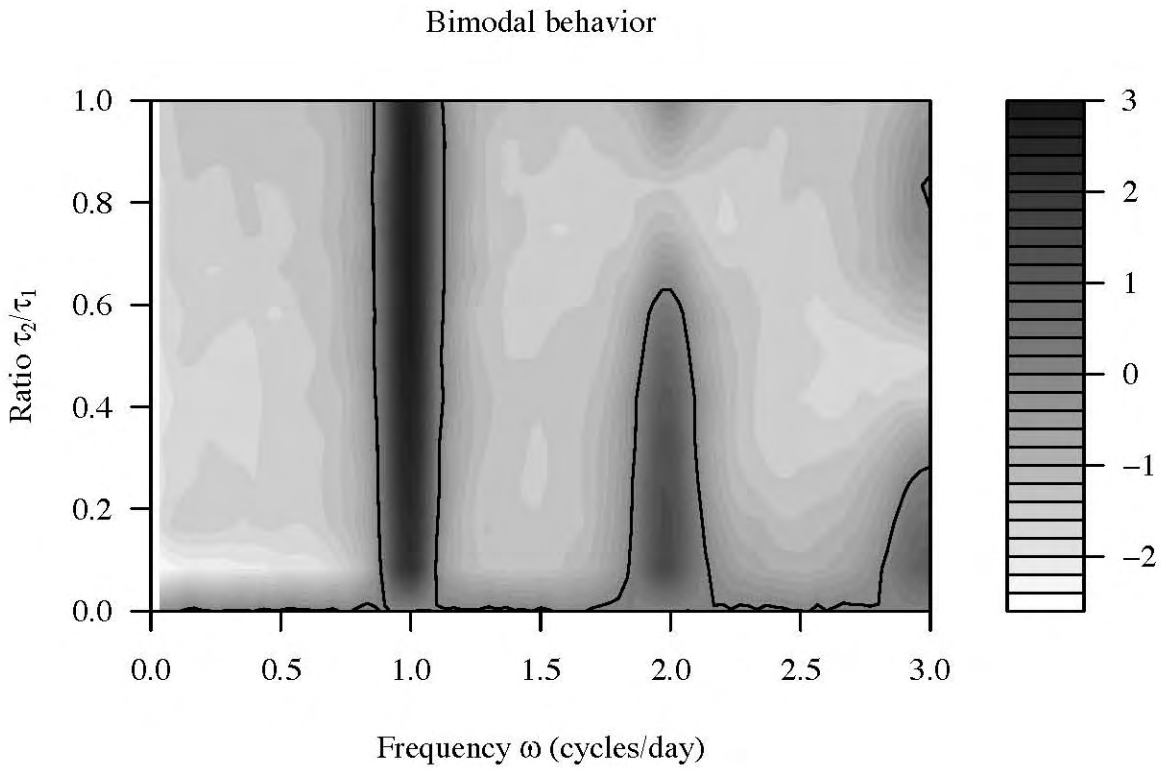

Figure A2. The natural logarithmic transformed averaged normalized periodograms from the same movement time series used in the analysis of Fig. 2 of the main text but with sampling interval at Δt = 4 hours.

Figure A3

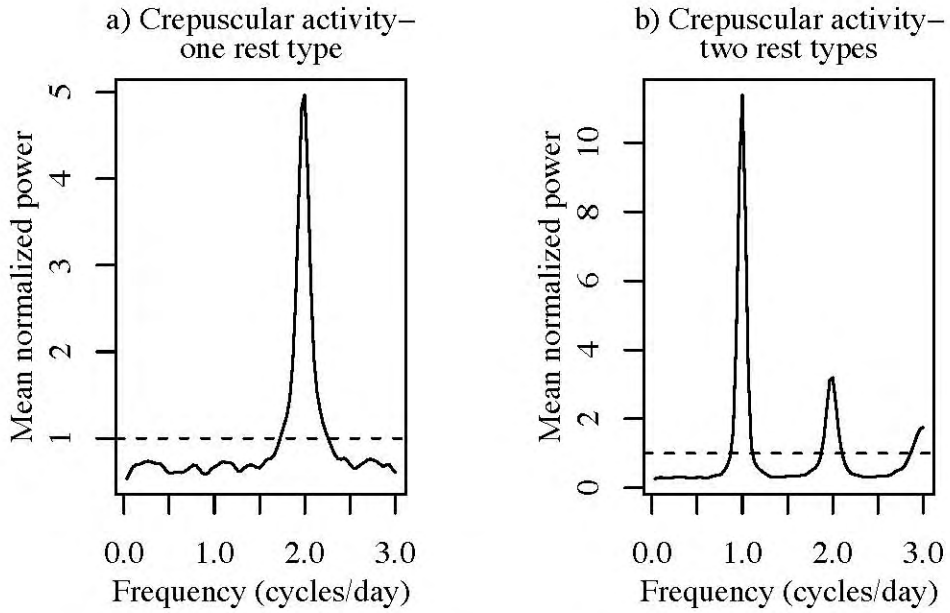

Figure A3. Periodograms for two kinds of crepuscular activity using the simulated data producing Figure 3 of the main text, but with sampling interval Δt = 4 hours. (a) For the "one rest type" activity, the daily behavioral sequence was defined by $S_K = \{\mathbf{m}_1, \mathbf{m}_3, \mathbf{m}_1, \mathbf{m}_3\}$ and E_K= {4, 8, 4, 8}, interpreted as alternating between rest and taxis. (b) The "two rest types" activity was defined by $S_K = \{\mathbf{m}_1, \mathbf{m}_3, \mathbf{m}_2, \mathbf{m}_3\}$ and E_K= {4, 4, 12, 4}, interpreted as the sequence rest, taxis, feed, taxis. The power spectrum in each Figure panel represents the average of 100 normalized periodograms. Horizontal dashed lines are drawn at the values for a theoretical white noise spectrum.

Figure A4

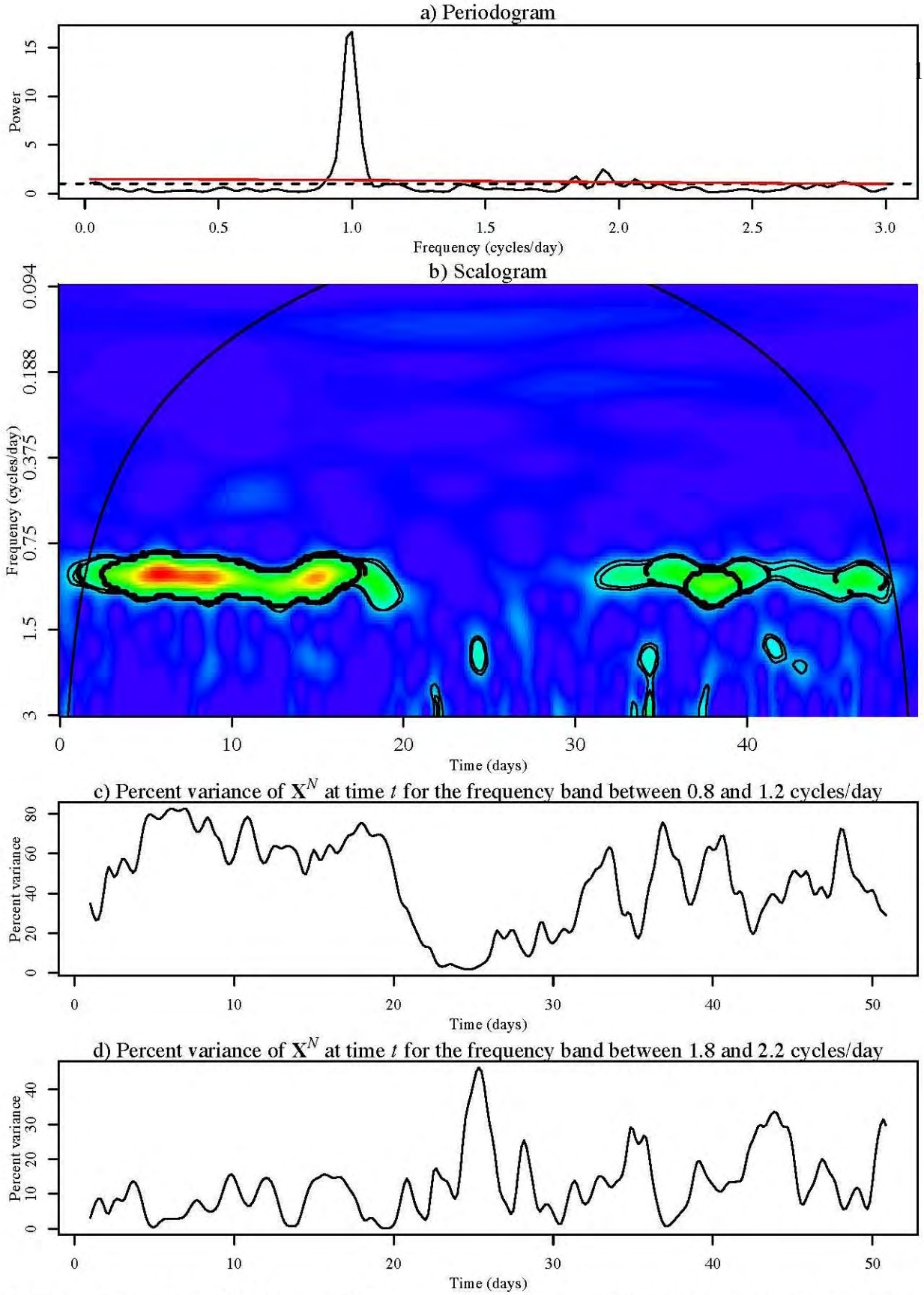

Figure A4. A reanalysis of the data analyzed in Fig. 4 (main text), but sampled at the coarser interval $\Delta t = 4$ hours. (a) The normalized smoothed periodogram shows peaks different from white (dashed lined) or red (red line) noise null models, suggesting cyclic behavior. (b) Using 1000 simulated step length time series based on the white and red noise null models, we calculated the bootstrapped 95th percentile significant patches, delineated by thin dashed and solid lines, respectively; significant patches remaining from an areawise test (see text) are delineated by thick dashed and solid lines for the white and red noise null models, respectively. The arched solid black line delineates the cone-of-influence. The bottom two panels show the time series of the percent variance explained by frequency bands around the (c) $\omega = 1$ cycle/day and (d) $\omega = 2$ cycles/day.

Figure A5

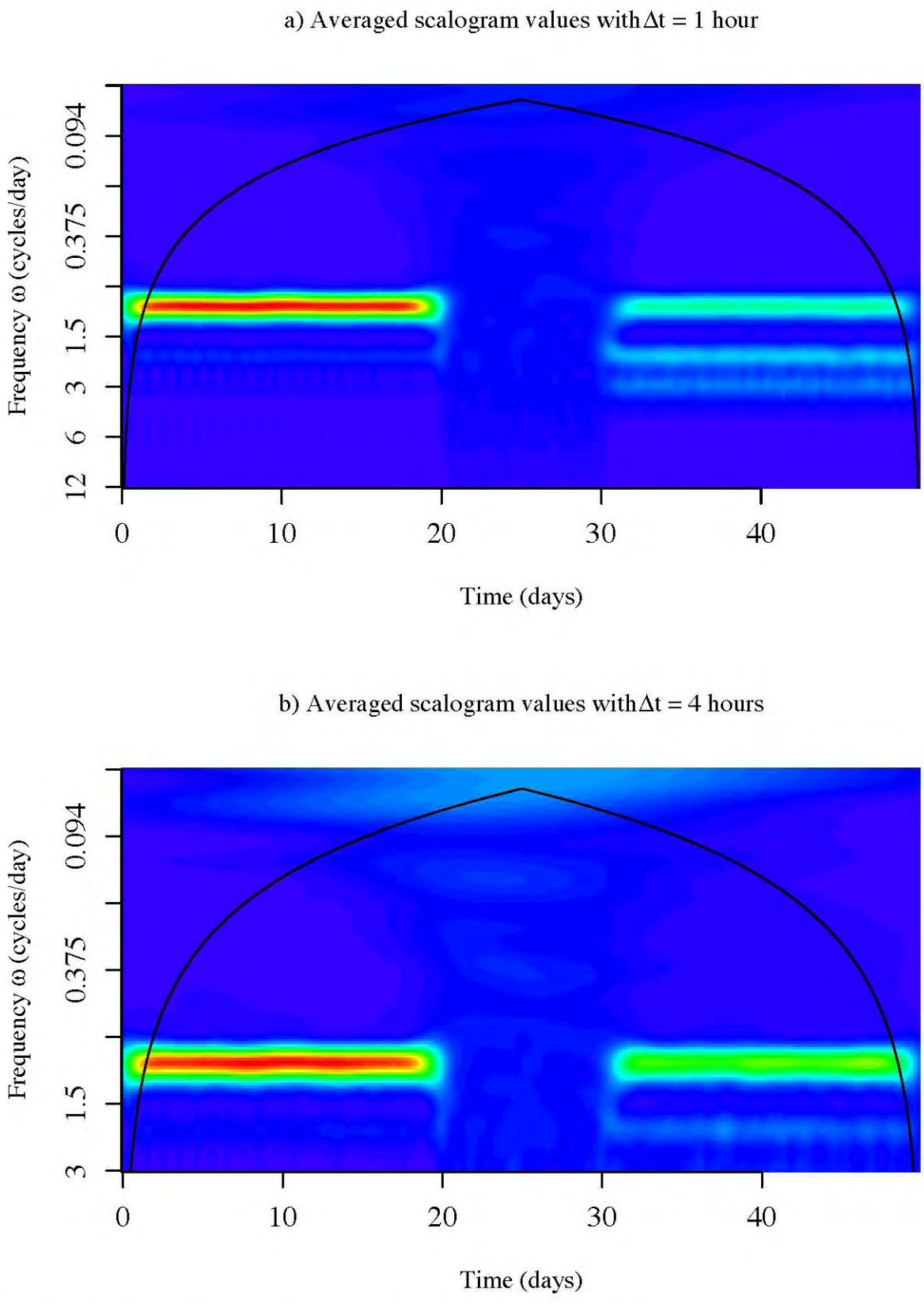

Figure A5. The contour of averaged scalogram values from 100 simulations using the daily behavioral sequence of Fig. 4 (main text) in the main with two sampling intervals, Δt = 1 hour (panel a), and Δt = 4 hours (panel b). The warm colors denote large values, and cool colors denote small values.

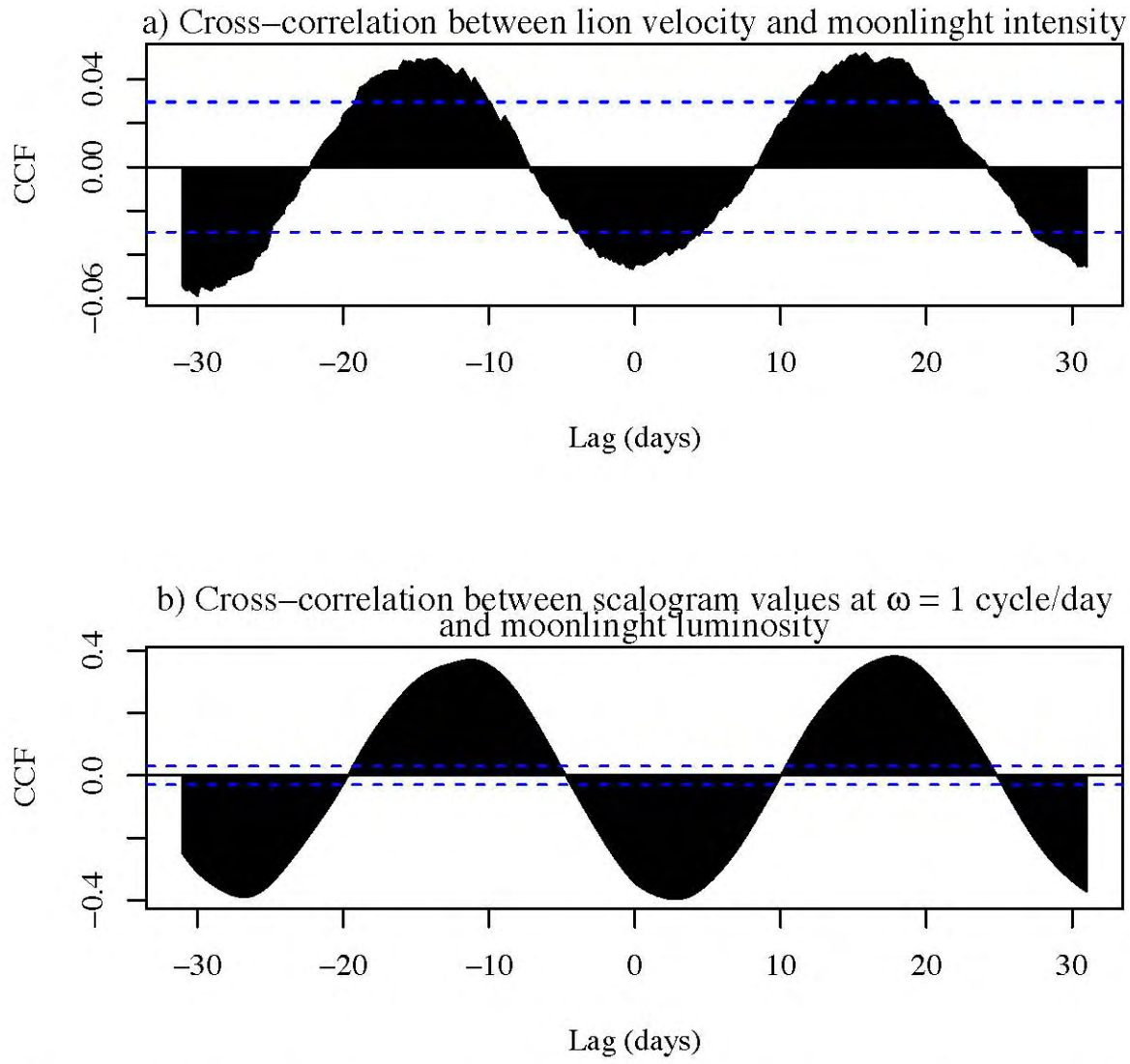

Figure A6. (a) cross-correlation estimates of the lion velocity and moonlight luminosity; (b) cross-correlation estimates of the scalogram modulus values at frequency $\omega = 1$ cycle/day and moonlight intensity. Horizontal blue dashed lines are drawn at $\pm 1.96/\sqrt{N-1}$, where N is the length of the velocity time series, which gives the approximate 95% confidence intervals of the Yule-Walker based estimates at each lag for white noise.

Figure A7

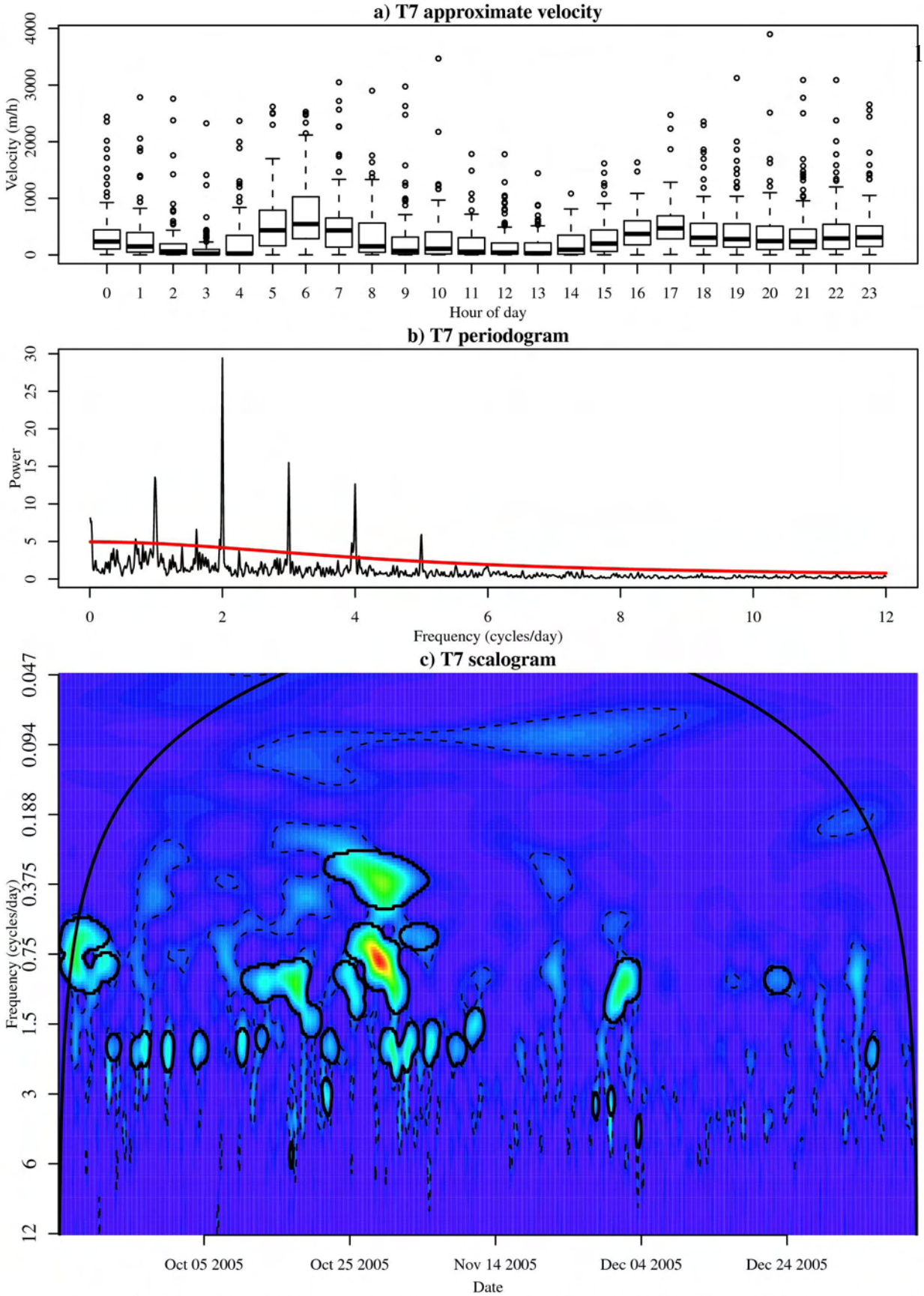

Figure A7. Based on the African buffalo data for T7 summarized in Table A1: (a) Box plots of velocity by hour of day; (b) the periodogram with theoretical spectrums of red noise shown by the solid red line and a white noise theoretical spectrum at 1; (c) Wavelet scalogram, where significant patches are defined as those that lie inside the solid black closed lines which delineate patch area remaining from an areawise test of patches defined by 95th estimated percentiles obtained from 1000 bootstrapped white noise null model time series, delineated by dashed lines. The arched solid black line delineates the cone-of-influence.

Figure A8

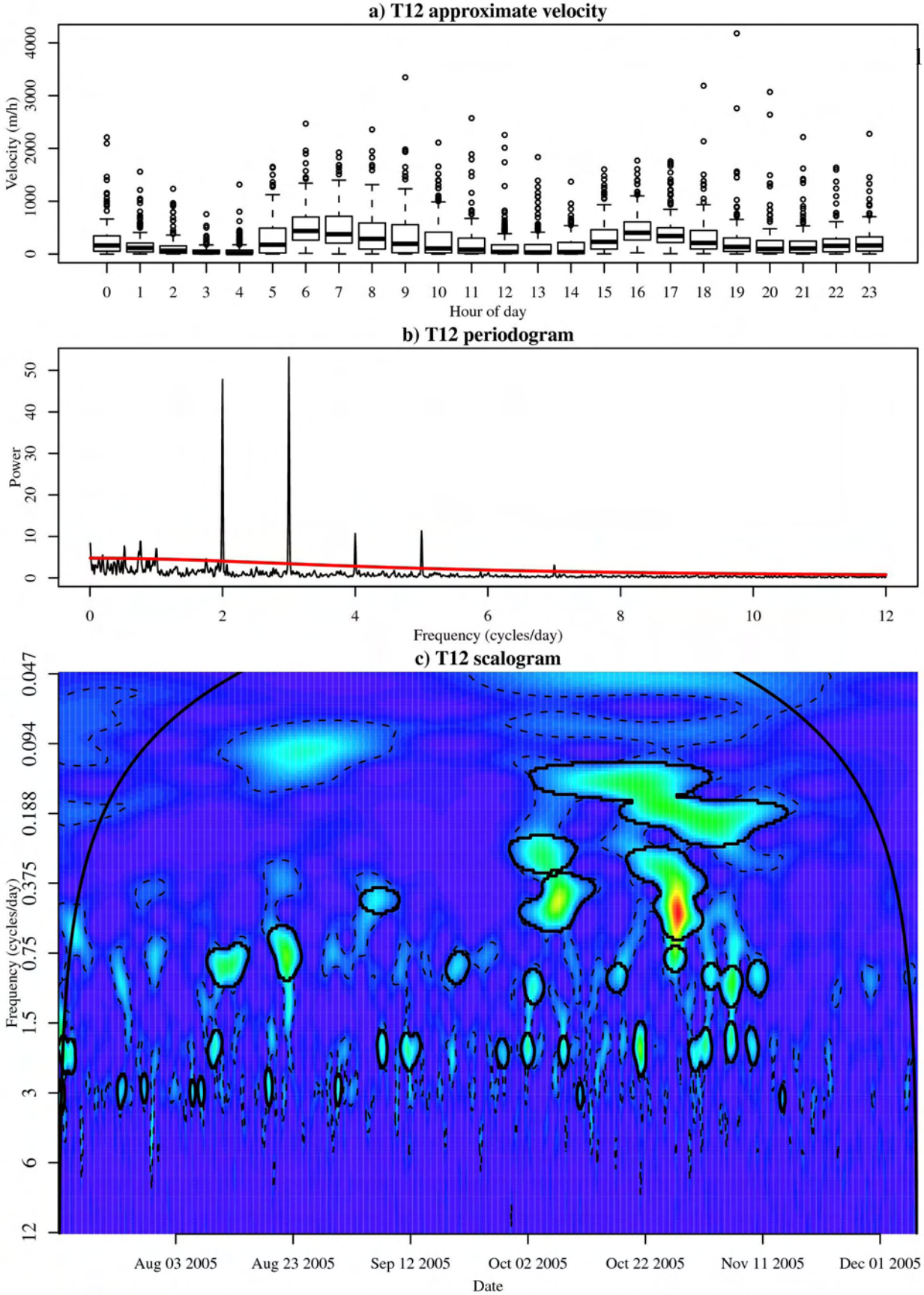

Figure A8. Based on the African buffalo data for T12 summarized in Table A1: (a) Box plots of velocity by hour of day; (b) the periodogram with theoretical spectrums of red noise shown by the solid red line and a white noise theoretical spectrum at 1; (c) Wavelet scalogram, where significant patches are defined as those that lie inside the solid black closed lines which delineate patch area remaining from an areawise test of patches defined by 95th estimated percentiles obtained from 1000 bootstrapped white noise null model time series, delineated by dashed lines. The arched solid black line delineates the cone-of-influence.

Figure A9

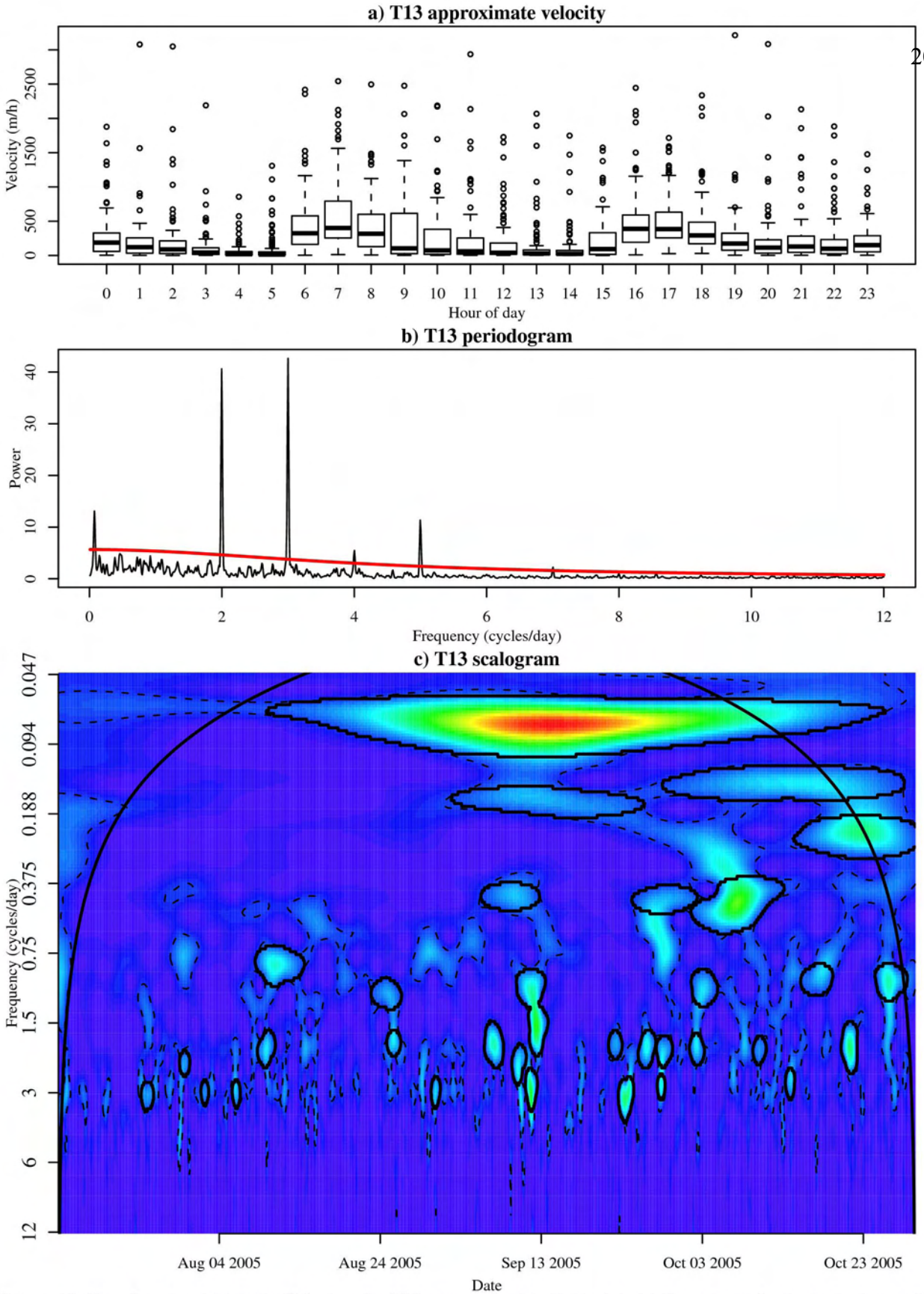

Figure A9. Based on the African buffalo data for T13 summarized in Table A1: (a) Box plots of velocity by hour of day; (b) the periodogram with theoretical spectrums of red noise shown by the solid red line and a white noise theoretical spectrum at 1; (c) Wavelet scalogram, where significant patches are defined as those that lie inside the solid black closed lines which delineate patch area remaining from an areawise test of patches defined by 95th estimated percentiles obtained from 1000 bootstrapped white noise null model time series, delineated by dashed lines. The arched solid black line delineates the cone-of-influence.

Figure A10

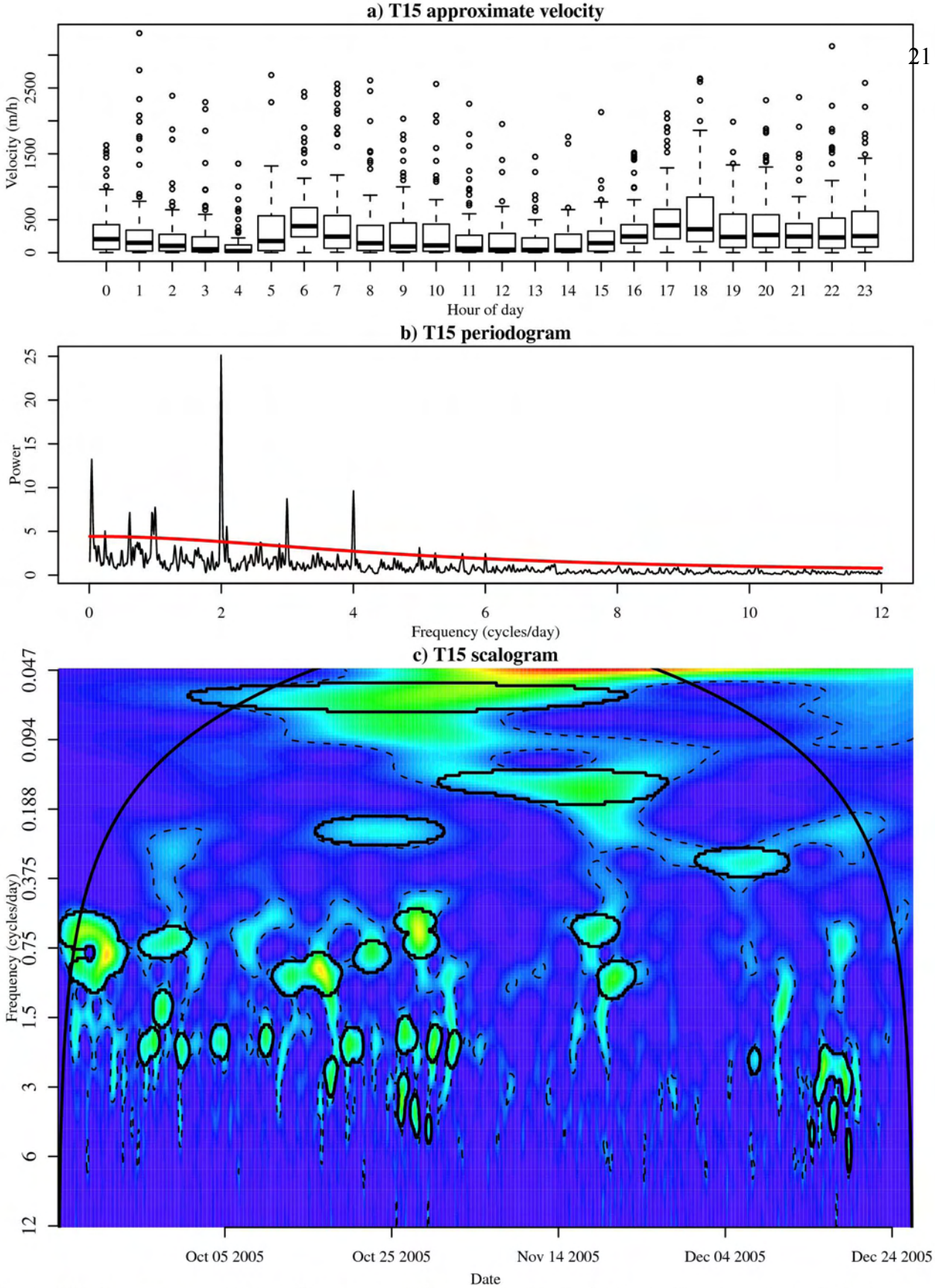

Figure A10. Based on the African buffalo data for T15 summarized in Table A1: (a) Box plots of velocity by hour of day; (b) the periodogram with theoretical spectrums of red noise shown by the solid red line and a white noise theoretical spectrum at 1; (c) Wavelet scalogram, where significant patches are defined as those that lie inside the solid black closed lines which delineate patch area remaining from an areawise test of patches defined by 95th estimated percentiles obtained from 1000 bootstrapped white noise null model time series, delineated by dashed lines. The arched solid black line delineates the cone-of-influence.

Figure A11

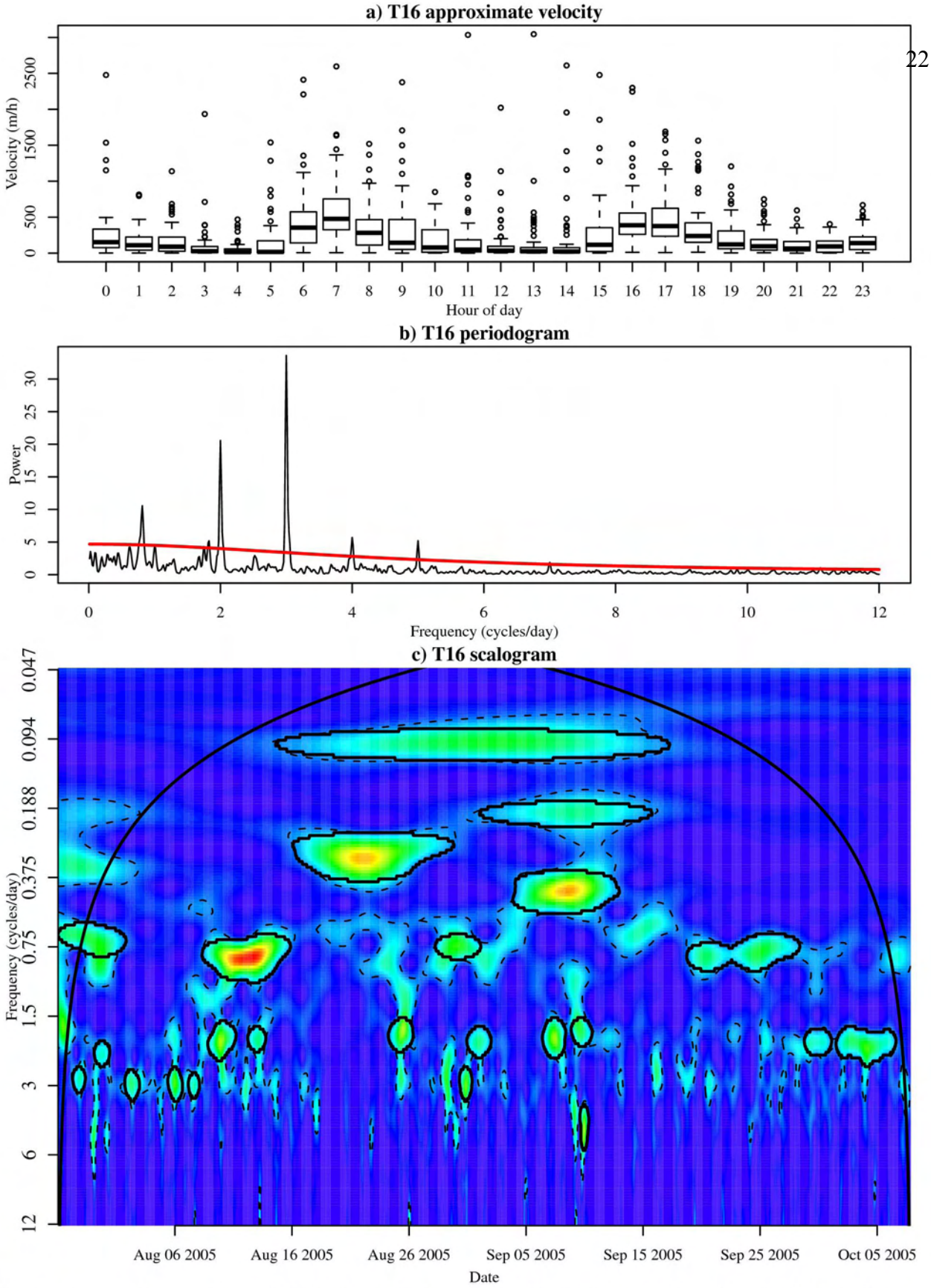

Figure A11. Based on the African buffalo data for T16 summarized in Table A1: (a) Box plots of velocity by hour of day; (b) the periodogram with theoretical spectrums of red noise shown by the solid red line and a white noise theoretical spectrum at 1; (c) Wavelet scalogram, where significant patches are defined as those that lie inside the solid black closed lines which delineate patch area remaining from an areawise test of patches defined by 95th estimated percentiles obtained from 1000 bootstrapped white noise null model time series, delineated by dashed lines. The arched solid black line delineates the cone-of-influence.

Figure A12

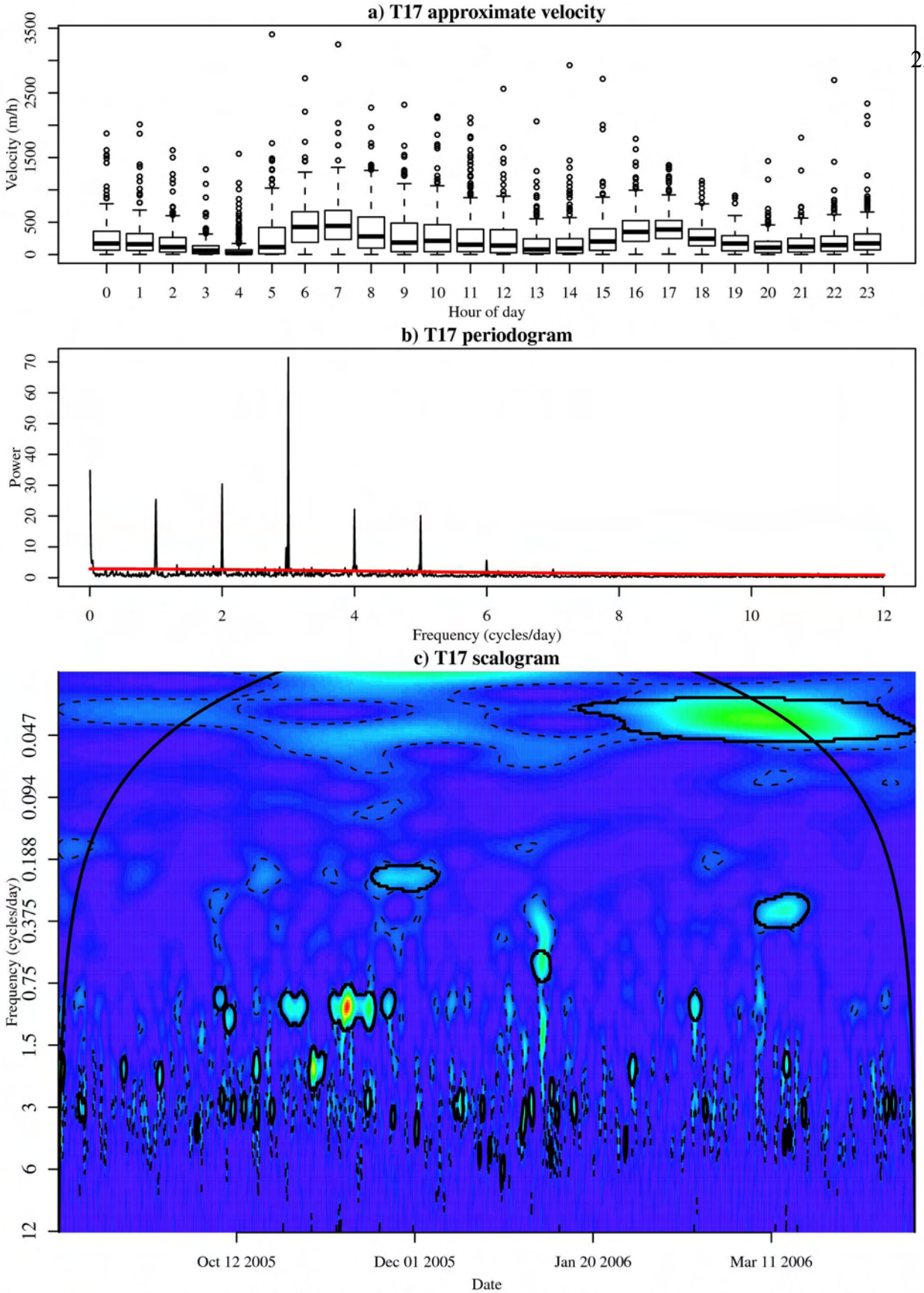

Figure A12. Based on the African buffalo data for T17 summarized in Table A1: (a) Box plots of velocity by hour of day; (b) the periodogram with theoretical spectrums of red noise shown by the solid red line and a white noise theoretical spectrum at 1; (c) Wavelet scalogram, where significant patches are defined as those that lie inside the solid black closed lines which delineate patch area remaining from an areawise test of patches defined by 95th estimated percentiles obtained from 1000 bootstrapped white noise null model time series, delineated by dashed lines. The arched solid black line delineates the cone-of-influence.

Figure A13

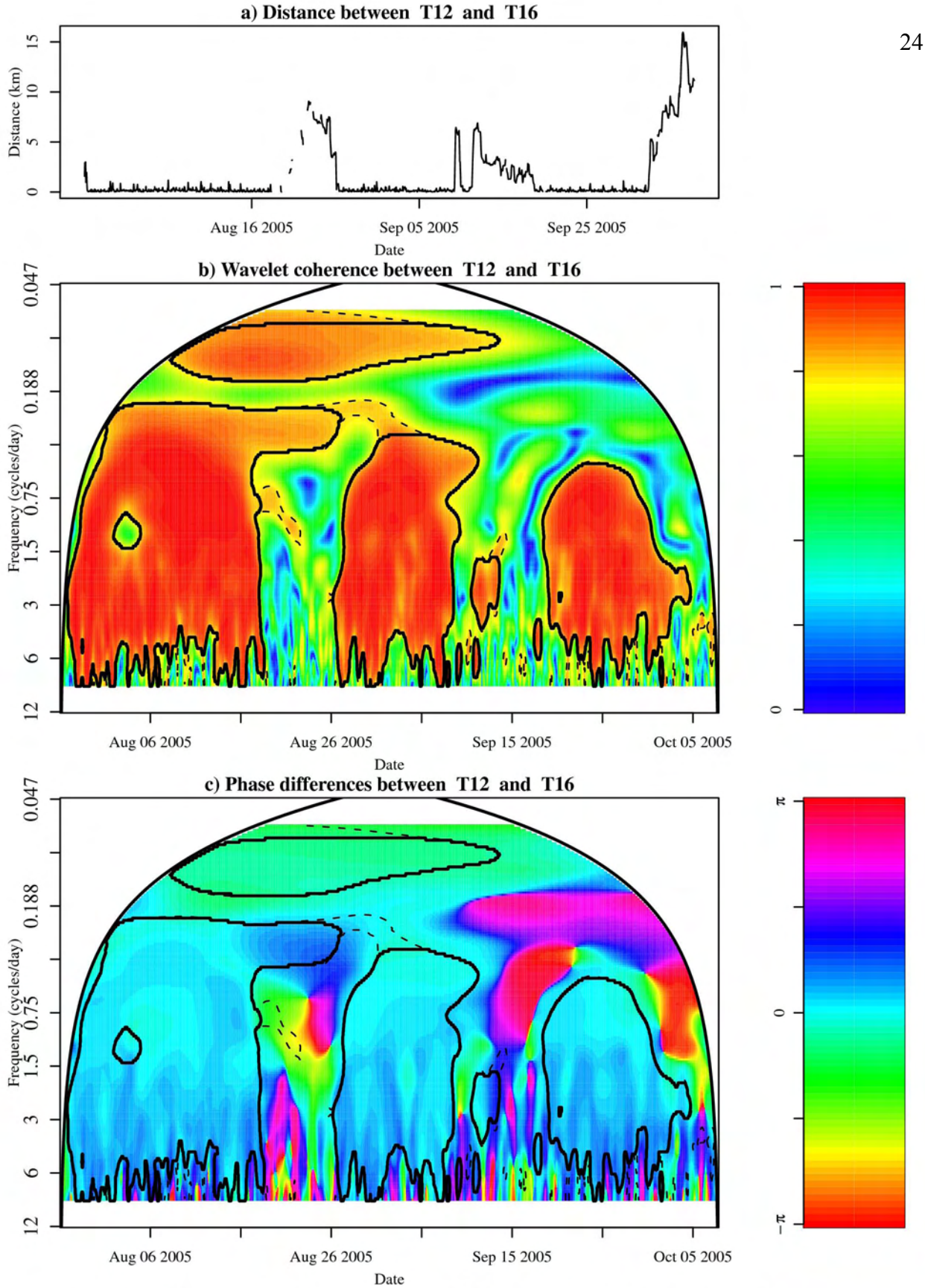

Figure A13. Based on the African buffalo data of T12 and T16 summarized in Table A1: (a) the distance between the pair, their wavelet coherency (b) and phase differences (c). Significant patches are defined as those that lie inside the solid black closed lines which delineate patch area remaining from an areawise test of patches defined by 95th estimated percentiles obtained from 1000 bootstrapped white noise null model time series, delineated by dashed lines, while the cone-of-influence is delineated by the arched solid black line.

Figure A14

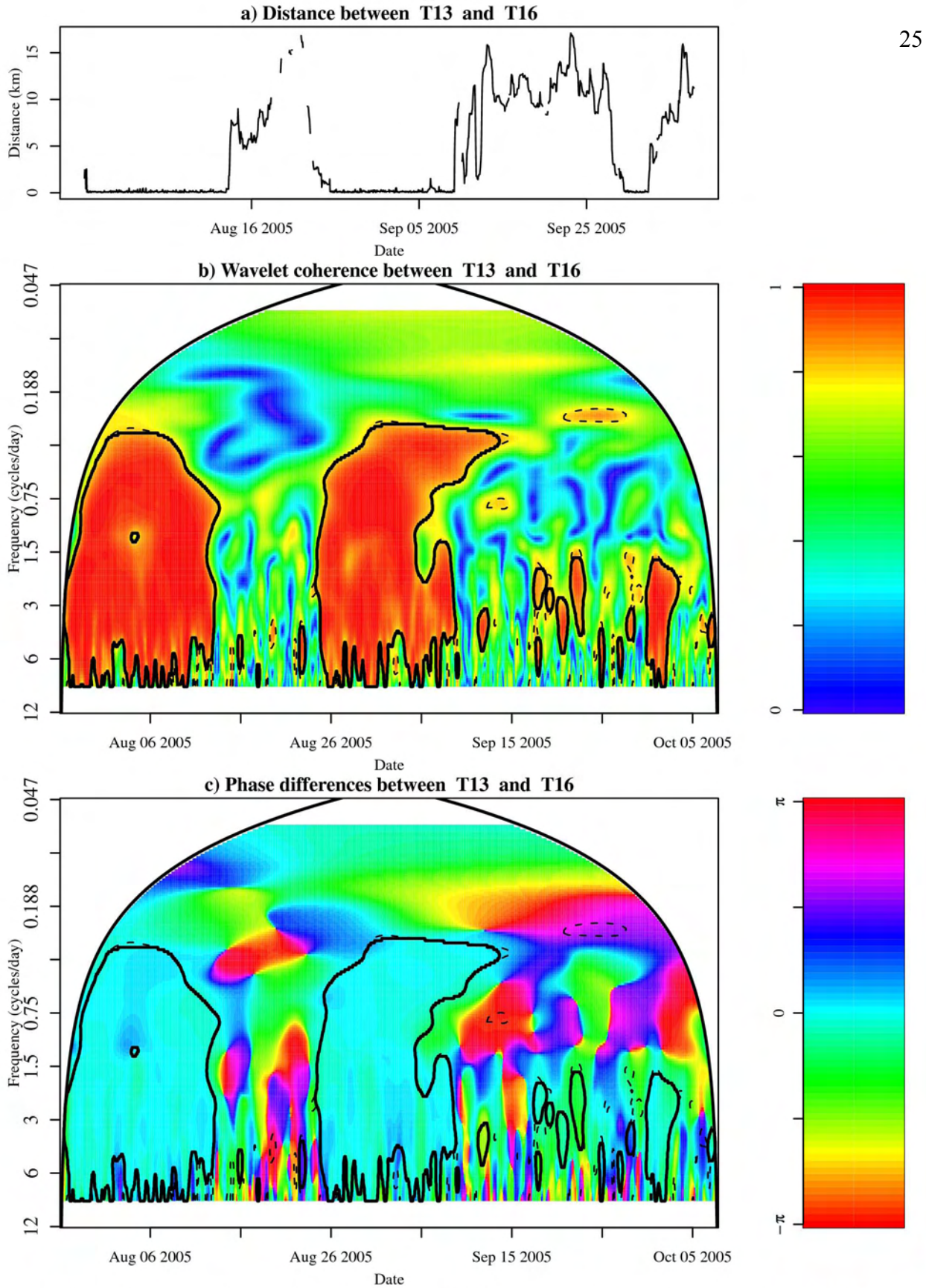

Figure A14. Based on the African buffalo data of T13 and T16 summarized in Table A1: (a) the distance between the pair, their wavelet coherency (b) and phase differences (c). Significant patches are defined as those that lie inside the solid black closed lines which delineate patch area remaining from an areawise test of patches defined by 95th estimated percentiles obtained from 1000 bootstrapped white noise null model time series, delineated by dashed lines, while the cone-of-influence is delineated by the arched solid black line.

Figure A15

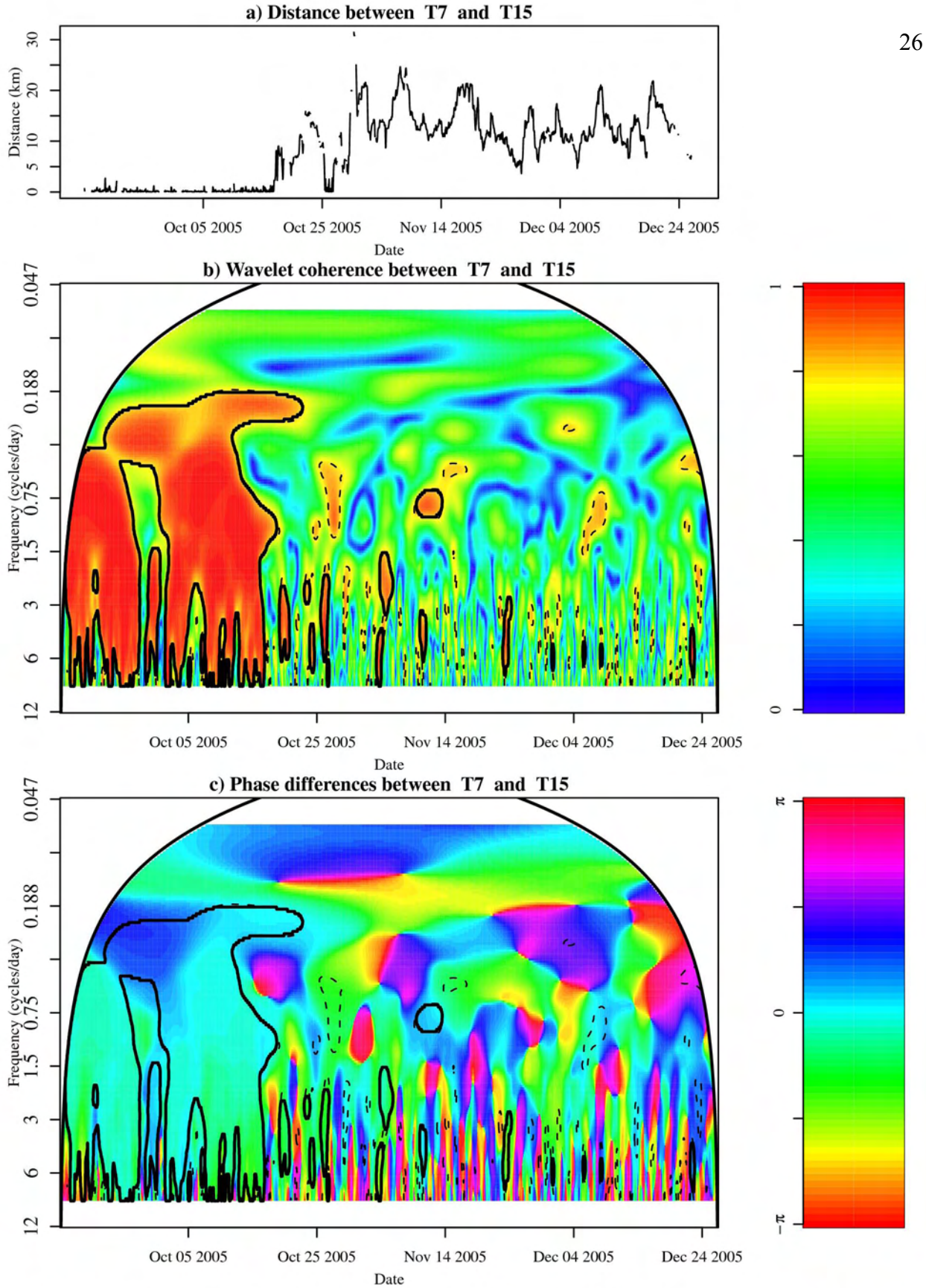

Figure A15. Based on the African buffalo data of T7 and T15 summarized in Table A1: (a) the distance between the pair, their wavelet coherency (b) and phase differences (c). Significant patches are defined as those that lie inside the solid black closed lines which delineate patch area remaining from an areawise test of patches defined by 95th estimated percentiles obtained from 1000 bootstrapped white noise null model time series, delineated by dashed lines, while the cone-of-influence is delineated by the arched solid black line.

Figure A16

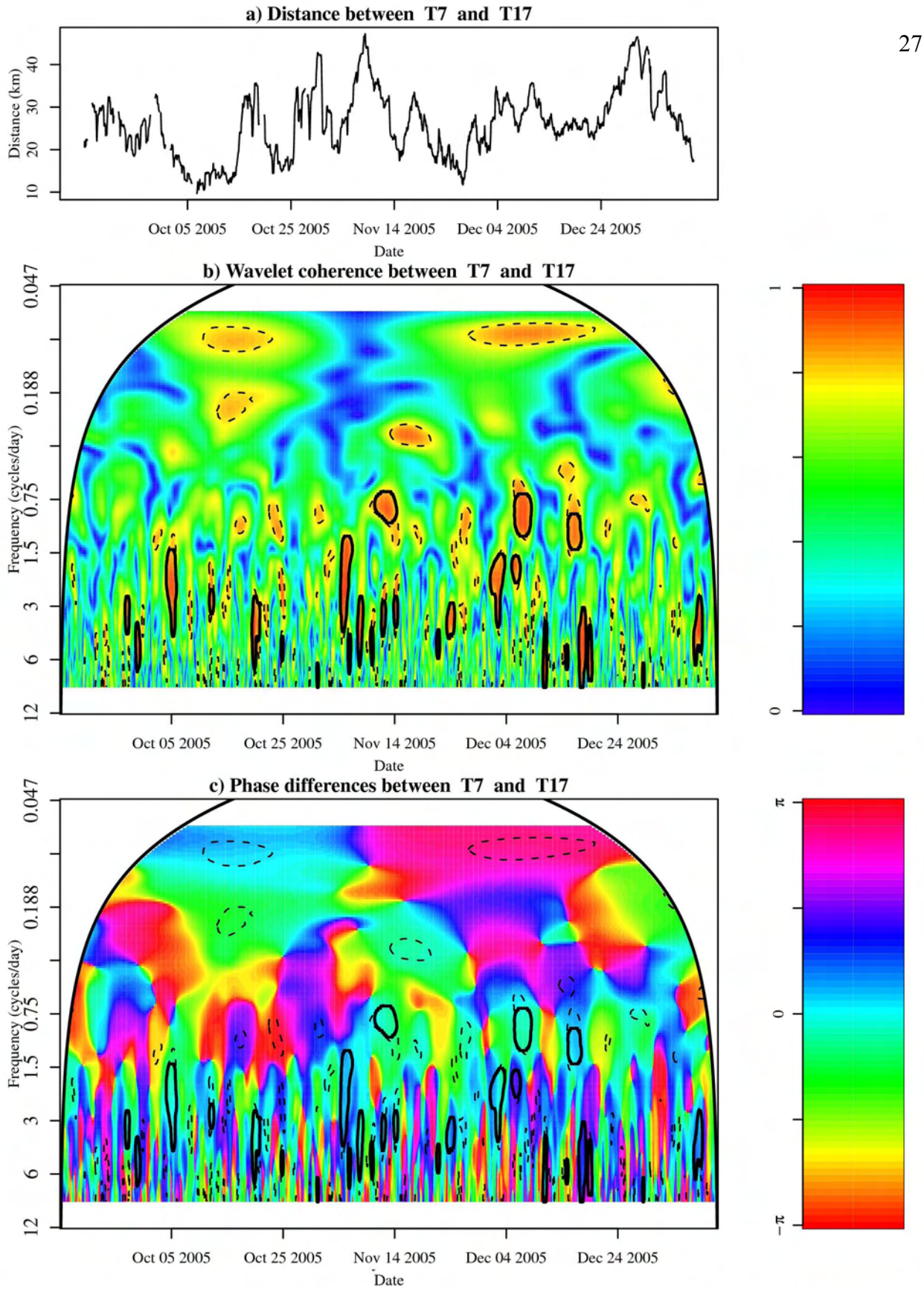

Figure A16. Based on the African buffalo data of T7 and T17 summarized in Table A1: (a) the distance between the pair, their wavelet coherency (b) and phase differences (c). Significant patches are defined as those that lie inside the solid black closed lines which delineate patch area remaining from an areawise test of patches defined by 95th estimated percentiles obtained from 1000 bootstrapped white noise null model time series, delineated by dashed lines, while the cone-of-influence is delineated by the arched solid black line.

Figure A17

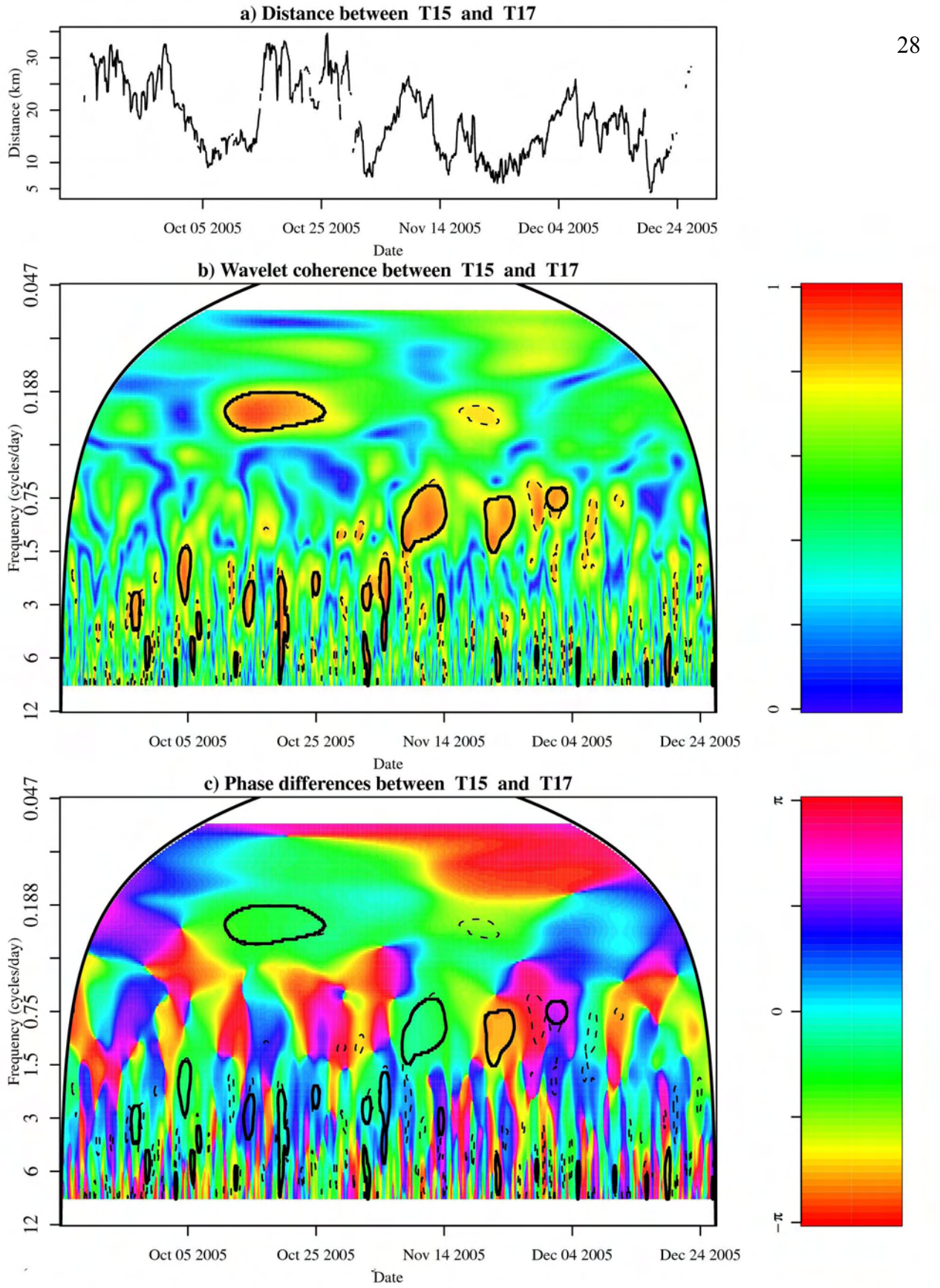

Figure A17. Based on the African buffalo data of T15 and T17 summarized in Table A1: (a) the distance between the pair, their wavelet coherency (b) and phase differences (c). Significant patches are defined as those that lie inside the solid black closed lines which delineate patch area remaining from an areawise test of patches defined by 95th estimated percentiles obtained from 1000 bootstrapped white noise null model time series, delineated by dashed lines, while the cone-of-influence is delineated by the arched solid black line.

Figure A18

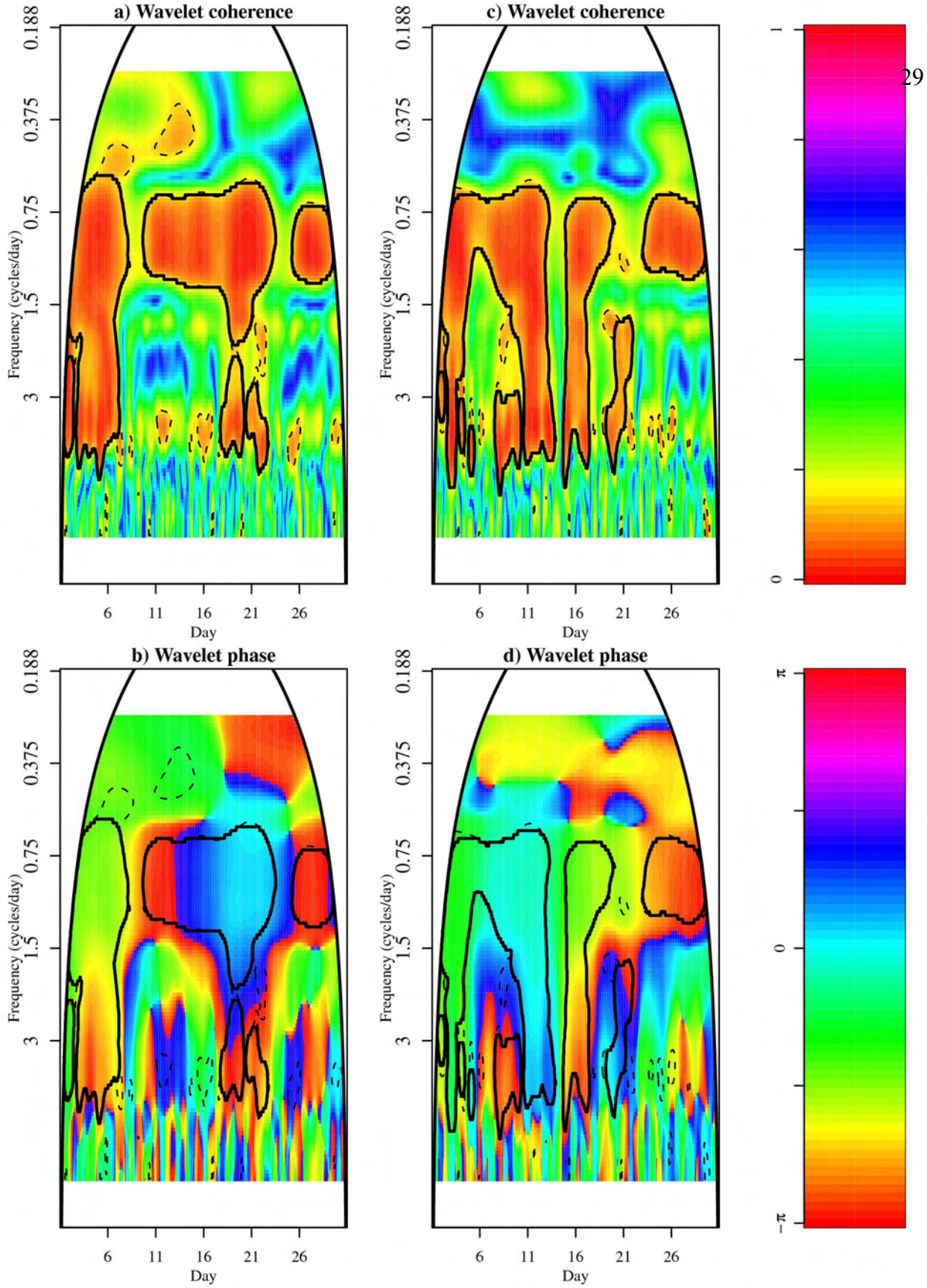

Figure A18. Using simulated movement with crepuscular activity and two types of rest periods as outlined in Fig. 3 of the main text, we calculated the wavelet cross coherency between one time series and two others. Panels (a) and (c) show the coherency, and panels (b) and (d) show the phase differences. In all panels, significant patches are defined as those that lie inside the solid black closed lines which delineate patch area remaining from an areawise test of patches defined by 95th estimated percentiles obtained from 1000 bootstrapped white noise null model time series, delineated by dashed lines, while the cone-of-influence is delineated by the arched solid black line. Even when coherence occurs spuriously, the phase differences are not consistently at any one value, and in particular, zero, in contrast with the empirical buffalo data sets. In addition, the buffalo show considerably more random daily behavioral activity (Table 1) than the simulation, which models a consistent crepuscular daily activity sequence

Figure A19

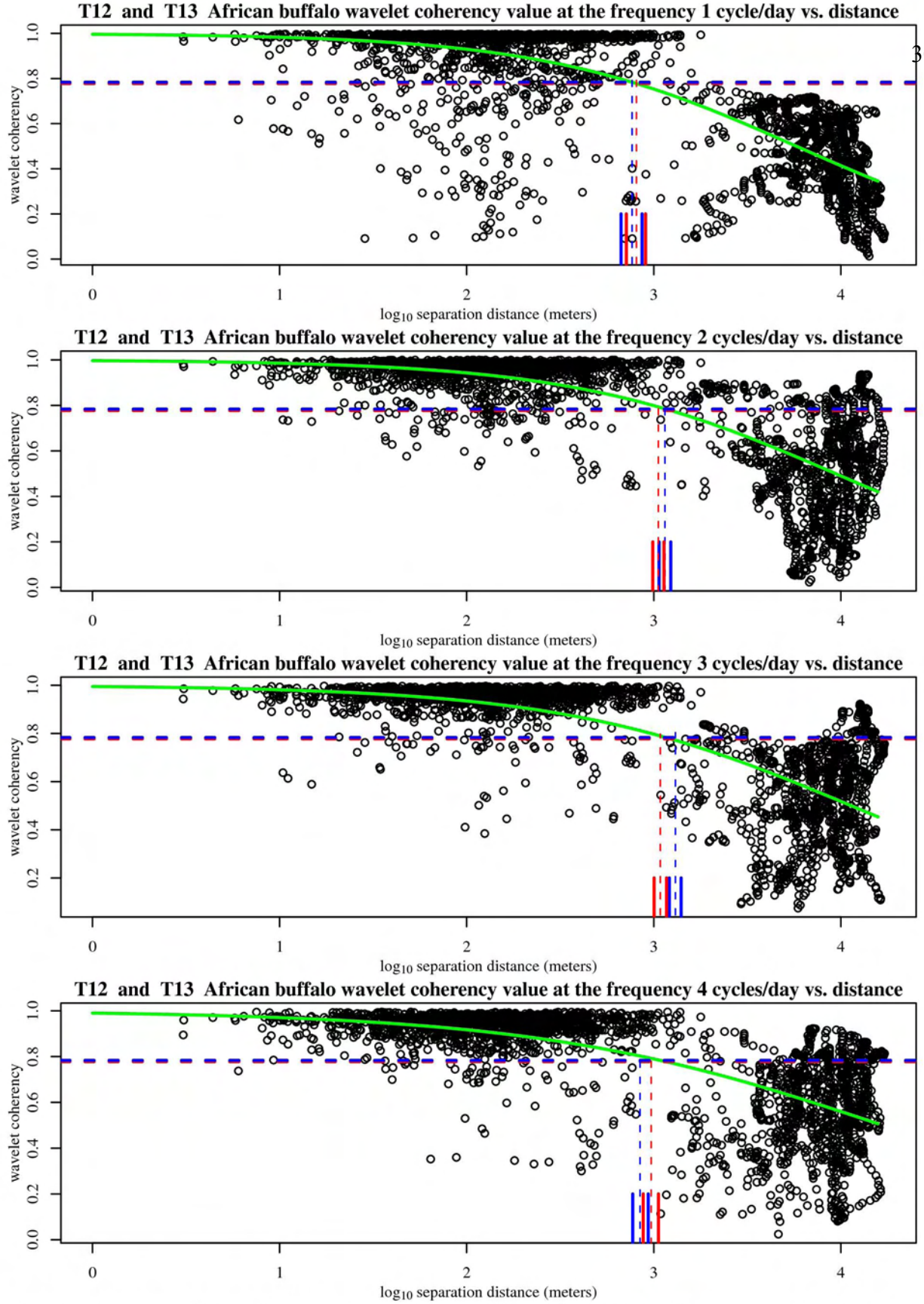

Figure A19. Based on the African buffalo data of T12 and T13 summarized in Table A1, plots of the coherency modulus values at frequency $\omega = 1$, $\omega = 2$, $\omega = 3$, and $\omega = 4$ cycles/day vs. distance between the two individuals are shown by the black circles. Solid curved green line shows the best fit sigmoidal curve, dashed horizontal red and blue lines show significant coherency values for red and white noise, respectively. Vertical dashed red and blue lines show the intersection with the red and white noise significance threshold, respectively, and the surrounding line stubs indicate the respective boundaries of the 95% confidence intervals from 1000 bootstrapped samples.

Figure A20

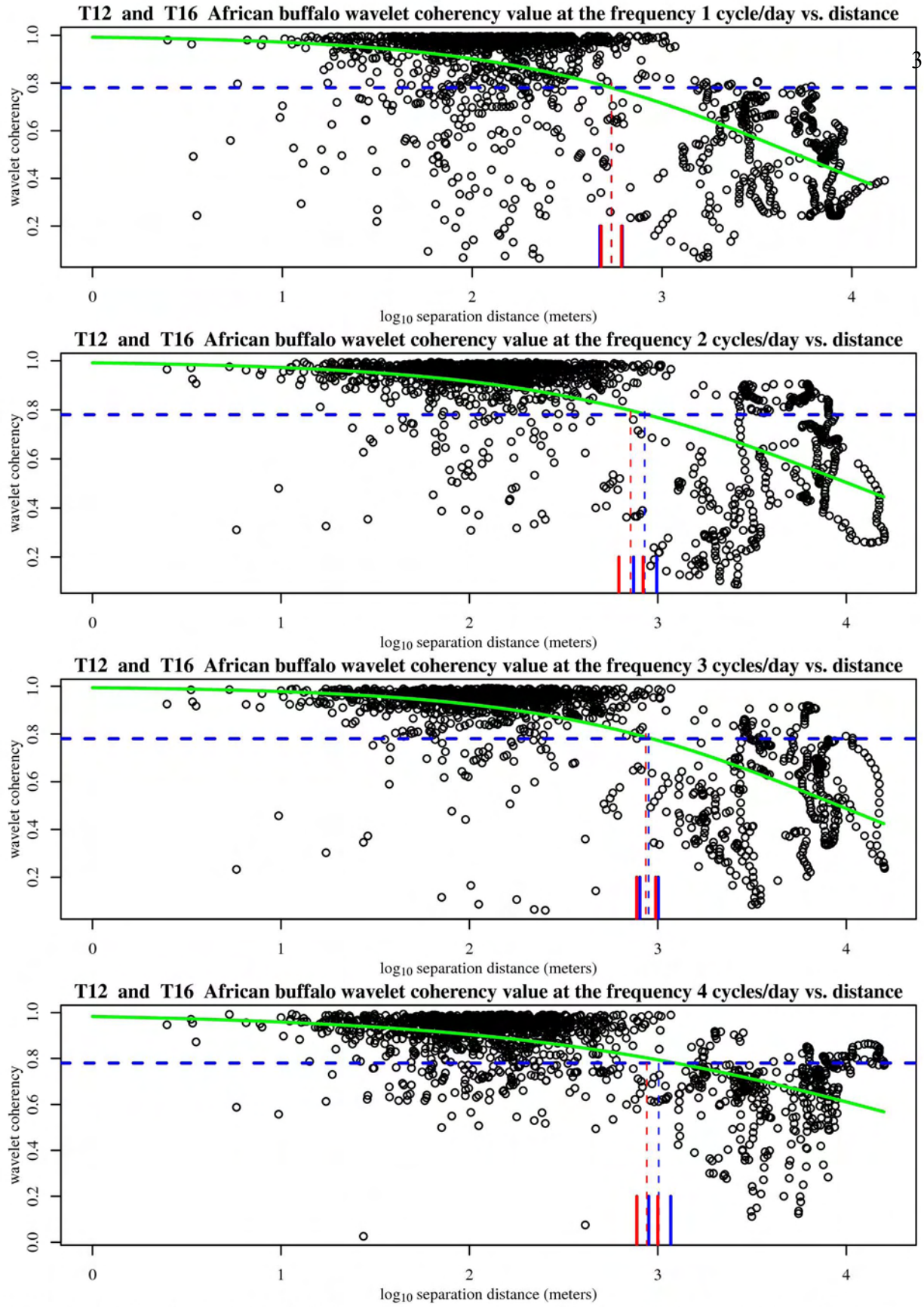

Figure A20. Based on the African buffalo data of T12 and T16 summarized in Table A1, plots of the coherency modulus values at frequency $\omega = 1$, $\omega = 2$, $\omega = 3$, and $\omega = 4$ cycles/day vs. distance between the two individuals are shown by the black circles. Solid curved green line shows the best fit sigmoidal curve, dashed horizontal red and blue lines show significant coherency values for red and white noise, respectively. Vertical dashed red and blue lines show the intersection with the red and white noise significance threshold, respectively, and the surrounding line stubs indicate the respective boundaries of the 95% confidence intervals from 1000 bootstrapped samples.

Figure A21

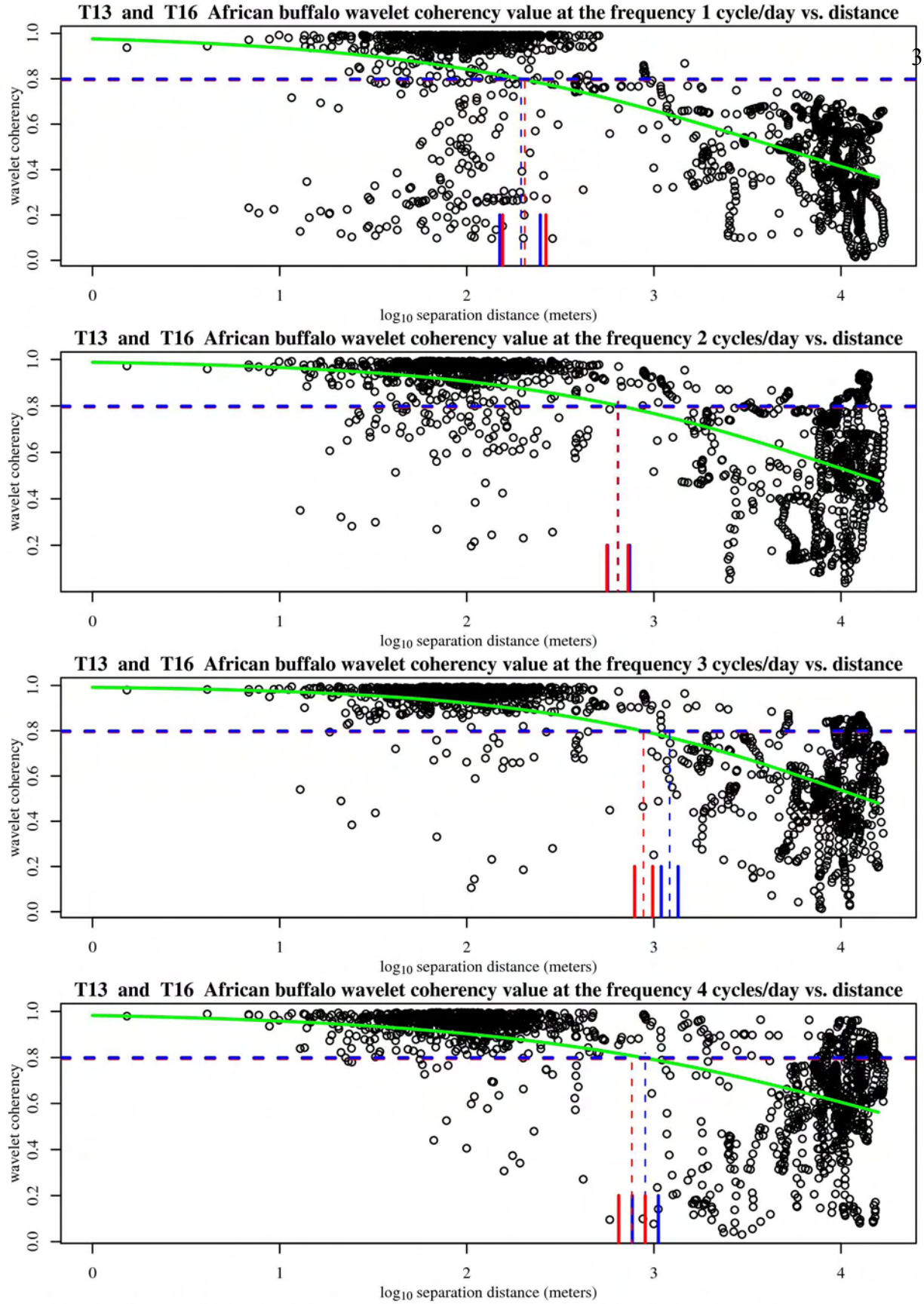

Figure A21. Based on the African buffalo data of T13 and T16 summarized in Table A1, plots of the coherency modulus values at frequency $\omega = 1$, $\omega = 2$, $\omega = 3$, and $\omega = 4$ cycles/day vs. distance between the two individuals are shown by the black circles. Solid curved green line shows the best fit sigmoidal curve, dashed horizontal red and blue lines show significant coherency values for red and white noise, respectively. Vertical dashed red and blue lines show the intersection with the red and white noise significance threshold, respectively, and the surrounding line stubs indicate the respective boundaries of the 95% confidence intervals from 1000 bootstrapped samples.

Figure A22

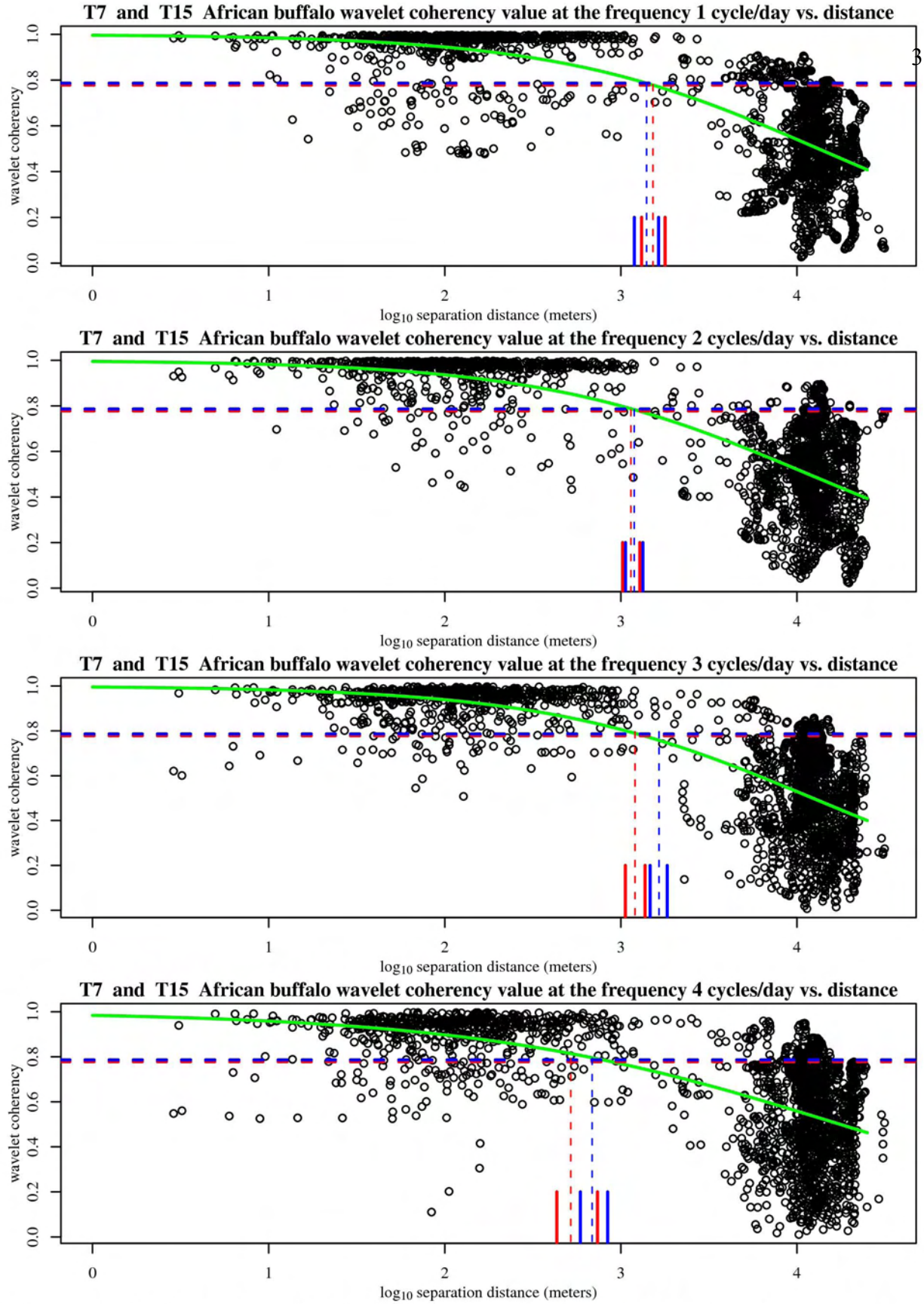

Figure A22. Based on the African buffalo data of T7 and T15 summarized in Table A1, plots of the coherency modulus values at frequency $\omega = 1$, $\omega = 2$, $\omega = 3$, and $\omega = 4$ cycles/day vs. distance between the two individuals are shown by the black circles. Solid curved green line shows the best fit sigmoidal curve, dashed horizontal red and blue lines show significant coherency values for red and white noise, respectively. Vertical dashed red and blue lines show the intersection with the red and white noise significance threshold, respectively, and the surrounding line stubs indicate the respective boundaries of the 95% confidence intervals from 1000 bootstrapped samples.